*materials*

MDPI

*Article*

# The Influence of Heat Treatment on the Tensile Creep Life of the TC25 Titanium Alloy

**Ang Tian [1,*], Jianglong Ma [1], Zhiguo Liu [2], Guangming Kong [2], Jiacheng Geng [1], Xinyuan Huang [1] and Guanliang Li [3,4]**

[1] School of Metallurgy, Northeastern University, Shenyang 110819, China; mjl15923484822@163.com (J.M.); gjc17863800508@163.com (J.G.); 20213625@stu.neu.edu.cn (X.H.)
[2] Naval Aviation University Qingdao Campus, Qingdao 266041, China; qdnuaalzg@163.com (Z.L.); guangmink@163.com (G.K.)
[3] Institute of Metal Research, Chinese Academy of Sciences, Shenyang 110016, China; glli22s@imr.ac.cn
[4] School of Materials Science and Engineering, University of Science and Technology of China, Shenyang 110016, China
* Correspondence: tiana@smm.neu.edu.cn; Tel.: +86-02483687735

**Abstract:** High-temperature titanium alloys are significant materials in the aerospace field, and their service life largely depends on creep aging. However, the creep behavior of the TC25 titanium alloy at high temperatures has not been reported. Here, the creep behavior of TC25 before and after heat treatment at 550 °C under different stresses was investigated. It was found that heat treatment significantly enhanced the creep resistance of the TC25 alloy. An increase in creep stress increased the steady-state creep rate and reduced creep life. The smooth αp/βtrans grain boundaries and refined αs improved creep resistance, and the creep mechanism changed from grain boundary sliding to dislocation climbing after heat treatment. This research provides theoretical data support for the application of the TC25 alloy at high temperatures.

**Keywords:** TC25 titanium alloy; heat treatment; creep behavior; creep fracture surface; creep mechanism

check for updates

**Citation:** Tian, A.; Ma, J.; Liu, Z.; Kong, G.; Geng, J.; Huang, X.; Li, G. The Influence of Heat Treatment on the Tensile Creep Life of the TC25 Titanium Alloy. *Materials* **2024**, *17*, 5821. https://doi.org/10.3390/ma17235821

Academic Editor: Jan Haubrich

Received: 24 October 2024
Revised: 9 November 2024
Accepted: 15 November 2024
Published: 27 November 2024

**Copyright:** © 2024 by the authors. Licensee MDPI, Basel, Switzerland. This article is an open access article distributed under the terms and conditions of the Creative Commons Attribution (CC BY) license (https://creativecommons.org/licenses/by/4.0/).

## 1. Introduction

High-temperature titanium alloys are widely used in jet engines as fan blades, compressor blades, and disks in order to improve the thrust–weight ratio of the engine and the maneuverability of the aircraft due to their characteristics of low density and high specific strength [1–5]. Creep failure is an important factor affecting the application of high-temperature titanium alloys [5,6], and creep performance at high temperatures is related to the microstructure [7,8]. Creep behavior, as an important indicator of reliability in the application of high-temperature titanium alloys, is a research hotspot of high-temperature titanium alloys [1]. The microstructure of high-temperature titanium alloys can be effectively improved through heat treatment, thereby altering their mechanical properties [9–11]. Nie et al. obtained the lamellar and equiaxed microstructures of TC18 by adopting different heat treatment methods, and their research indicated that TC18 had better creep resistance [11]. Therefore, conducting research on the impact of the microstructure of high-temperature titanium alloys before and after heat treatment on creep life and creep mechanisms is essential.

In recent years, the influence of microstructure on the creep properties of high-temperature titanium alloys has aroused extensive research interest [11–16], and the creep of two-phase titanium alloys was mainly attributed to the slip of individual phases as well as the slip across phase boundaries [17]. It has been reported that a lamellar microstructure has better creep resistance than an equiaxed microstructure [11,18], and the creep resistance of basket-weave microstructure is superior to that of biphasic microstructure [14,15]. This has prompted many researchers to elucidate the relationship between microstructure and creep properties, proposing many typical creep mechanisms, such as dislocation

gliding [8,11,15], grain boundary slip [19–21], twinning [1,22,23], and the precipitation of silicides [1,3,7]. Gu et al. indicated that the creep of TC11 at 450–550 °C was influenced by dislocation movement [15], and Zhang et al. showed that the creep mechanism of Ti65 in the transverse direction was grain boundary slip [20]. It is of vital importance to study the influence of the microstructure of different titanium alloys on creep properties and the corresponding creep mechanisms.

The TC25 alloy (the nominal composition is Ti-6.5Al-2Mo-1Zr-1Sn-1W-0.2Si) is a thermal-strength (α + β) biphasic titanium developed by the former Soviet Union in 1971 [24–26]. And due to the addition of the β-eutectoid element W and neutral element Sn, it has exhibited excellent mechanical properties at service temperature (at least 550 °C) [25,26]. He et al. [24] investigated the microstructure evolution of TC25 following deformation and heat treatment and indicated that the volume fraction of the globularized α phase increases with increasing deformation, and the amount of Mo in α phase decreases with globularization. Zhang et al. [27] studied the fatigue life of equiaxed, bimodal, and lamellar microstructures of TC25 and demonstrated that equiaxed and bimodal microstructures exhibited greater high-cycle fatigue resistance than the lamellar microstructure. Little research, however, has focused on the effects of heat treatment on the creep properties and creep mechanisms of TC25.

In this study, the microstructure change, tensile creep properties, and creep mechanism of TC25 before and after heat treatment at 550 °C were systematically studied. This work helps to comprehend the effect of heat treatment on the microstructure of TC25 titanium alloys, as well as the influence of microstructure on the tensile creep life and mechanism of TC25 titanium alloys. It has a certain guiding significance for the application of TC25 titanium alloys under high-temperature conditions.

## 2. Materials and Methods

### *2.1. Materials*

The experimental materials used in this study were purchased commercially (Shenyang Enyiyou Technology Co., Ltd., Shenyang, China) and produced through vacuum arc melting, forging, and rolling. The chemical composition is listed in Table 1. The obtained materials were divided into two groups. One group remained in the original state (hereinafter referred to as TC25-1), and the other group was further subjected to solution treatment and aging treatment (hereinafter referred to as TC25-2). The (α + β)/β phase transition temperature (Tβ) of this alloy was 1018 °C [20,27], determined by high-temperature differential thermal analyzer. The heat treatment procedure for TC25-2 was solution treatment at 960 °C (below $T_\beta$) for 2 h, followed by air-cooling to room temperature, and then aging at 550 °C for 3 h, followed by air-cooling to room temperature. Argon gas was used as the protective gas during the solution treatment and aging processes.

**Table 1.** Chemical composition of TC25 alloy (wt. %).

| Ti | Al | W | Zr | Mo | Sn | Si |
|---|---|---|---|---|---|---|
| Bal. | 6.48 | 0.72 | 1.02 | 1.78 | 1.12 | 0.13 |

### *2.2. Experimental Procedures*

In order to investigate the influence of microstructure on the tensile creep behavior of TC25-1 and TC25-2, wire cutting was performed on the two groups of materials. Figure 1 shows the processing details of the cylindrical specimen, with a gage length of 25 mm and a diameter of 5 mm [27]. The tensile creep tests were carried out on an electronic high-temperature creep testing machine (TSC105B, WANCE, Shenzhen, China). During the entire testing process, the whole specimen was kept at a constant temperature of 550 ± 2 °C in an electric resistance heating furnace [11]. Three kinds of stress, 500 MPa, 550 MPa, and 610 MPa, were applied in this study, and a prestress of 190 N was applied at each creep heating-up and heat preservation stage. In the electric resistance heating furnace, the specimen was heated to

the designed test temperature with a heating rate of 5 °C/min and held for 1 h to stabilize the temperature over the gage section. The displacement and time data were collected during the testing process using the TestPilot_HTC_D01C version 1.0.1106 data collection and control software. All tests were not stopped until the specimen ruptured.

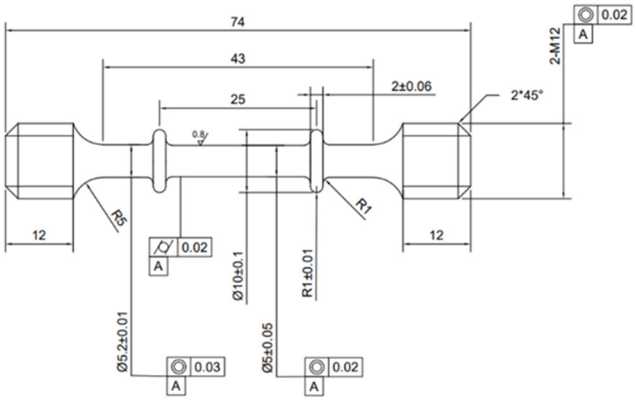


**Figure 1.** Geometric shape and dimensions of the tensile creep specimens (in mm).

### *2.3. Microstructure Characterization*

In order to reveal the effect of heat treatment on the TC25 alloy microstructure and the creep mechanism at 550 °C, various observational experiments were conducted. X-ray diffraction (XRD, Rigaku SmartLab 9Kw, Tokyo, Japan) equipped with Cu-Kα was used to identify the phase composition, with a scanning speed of 10°/min. An optical microscope (OM, Olympus GX71, Tokyo, Japan) and a scanning electron microscope (SEM, JEOL JSM-7800F, Tokyo, Japan) were used to observe the microstructure of the materials. The working voltage of the SEM was 15 KV, and the LDF mode was adopted. An energy-dispersive spectrometer (EDS, OXFORD XMAX 20, Britain, UK) was used to determine the element distribution. Meanwhile, backscatter diffraction was used to analyze the local orientation difference (EBSD, SYMMETRY S2, Britain, UK). The specimens for OM and SEM characterization were polished with a series of abrasive papers (#400-3000) and then chemically etched in corrosive liquid with a volume ratio of $HF/HNO_3/H_2O$ = 1:3:7 [28]. The chemical etching time is about 1~2 s. After the etching, the specimens were ultrasonically cleaned in alcohol for 5 min. The EBSD specimens were polished with a series of abrasive papers and then thinned by argon ion, while the creep fracture surface was cleaned with alcohol and observed by SEM.

## 3. Results and Discussion

### *3.1. Initial Microstructure*

The XRD results of TC25 before and after heat treatment are presented in Figure 2. It can be seen from Figure 2 that the main diffraction peaks of TC25 before and after heat treatment corresponded to α-titanium and β-titanium, which indicates that TC25 is mainly composed of the α and β phases [27]. The integral intensity of diffraction peaks is proportional to the volume fraction of the corresponding phase [29,30]. The relative intensity of the (110) diffraction peak (β-titanium) in TC25-2 is significantly lower than that in TC25-1, indicating that there is a transformation from the β phase to α phase during the heat treatment process [31,32].

It has been reported that titanium alloys (TC25) which are used at high temperatures have bimodal structures composed of equiaxed primary α phase (αp) and transformed β matrix (βtrans); in particular, the β matrix (βtrans) consists of β ligaments and secondary α laths (αs) [33]. Figure 3a,b show the OM microstructures of TC25-1 and TC25-2; both TC25-1 and TC25-2 exhibit a typical bimodal microstructure in terms of $\alpha_p$ and $\beta_{trans}$ phases. The heat treatment process made the adjacent $\alpha_p$ in TC25-1 grow to a larger $\alpha_p$ with a long elliptical shape in TC25-2. Image pro plus 6.0 was used to quantitatively analyze the content of $\alpha_p$ before and after heat treatment. The percentage content of $\alpha_p$ in TC25-1 is 51.8%, and

that in TC25-2 is 55.7%. The increase in $\alpha_p$ content after heat treatment indicated that there was a transformation from the $\beta_{trans}$ to $\alpha_p$ during the heat treatment process, which further confirmed the results of XRD patterns in Figure 2. Figure 3c,d show the enlarged TC25-1 and TC25-2 microstructure, respectively. It can be clearly observed that $\beta_{trans}$ is filled with a large amount of $\alpha_s$ by bright contrast. After heat treatment, in TC25-2, $\alpha_s$ became thinner, presenting a needle-like microstructure, and arranged in parallel in multiple directions. The patterns of the $\alpha_s$ phase could be observed clearly after local magnification as Figure 3e,f showed, and the transformation from $\beta_{trans}$ to $\alpha_p$ during the heat treatment process could also be obtained. In addition, small spherical precipitates were found in TC25-1 (the red dashed circle in Figure 3e), while no obvious precipitates were found after heat treatment, and the precipitates are mainly silicides [34–36], as the mapping results show in Figure 3g.

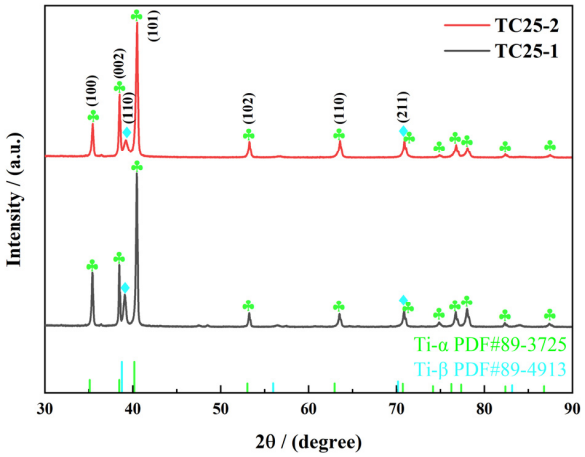


**Figure 2.** XRD patterns of TC25-1 and TC25-2 (the square represents Ti-α, and the club represents Ti-β).

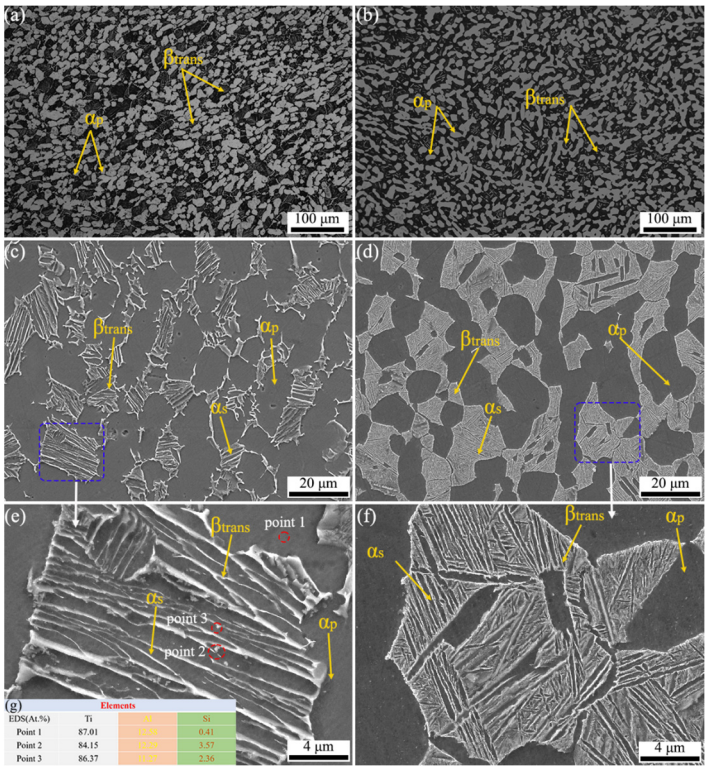


**Figure 3.** The microstructure of TC25-1 and TC25-2: (**a**,**b**) OM microstructure; (**c**,**d**) SEM microstructure; (**e**,**f**) regional amplification diagram (the blue dash line boxes in (**c**,**d**)); (**g**) elemental mapping in the red area of (**e**).

### 3.2. Tensile Creep Behavior

In order to evaluate the creep resistance of the alloy, creep tests were conducted at 550 °C under three different stresses (500 MPa, 550 MPa, 610 MPa). Creep is a temperature-sensitive thermal activation process that is generated by the combination of dislocation motion, atomic thermal motion, and stress [11,37]. The creep process is generally divided into three stages. Firstly, in the decelerating creep stage, plastic deformation and work hardening occurred in the alloy. Secondly, the steady-state creep stage is mainly caused by the cooperation of dislocations and obstacles, as well as the dislocation climb and slip [38]. Finally, in the third stage (accelerating creep stage), the creep rate increases sharply, and the creep damage continues to accumulate until the material fractures. Usually, the steady-state creep rate and creep rupture life are used to evaluate the creep resistance of materials [3,39].

Figure 4 displays the creep properties of TC25-1 and TC25-2. As Figure 4a shows, the curve indicates that under 610 MPa, the TC25-1 alloy had no obvious decelerating creep and steady-state creep stages, only an obvious accelerating creep stage. However, after heat treatment, there are obvious three creep stages, as Figure 4c shows. The steady-state creep stage accounts for approximately 20% (10 h) of the entire creep stage. Otherwise, it could be concluded that the TC25-1 remains with the accelerated creep stage as the main stage, and the steady-state creep stage emerges at 550 MPa and 500 MPa. The steady-state creep stage (550 MPa and 500 MPa) occupied 4% (2 h) and 12.5% (25 h) of the entire creep stage, respectively. For TC25-2, the steady-state creep stage accounts for 17% (20 h) and 18% (35 h) of the entire creep stage at 550 MPa and 500 MPa, respectively. In addition, under the high-stress conditions (610 MPa, 550 MPa), the creep life of TC25-2 (58 h, 128 h) exceeds twice that of TC25-1 (21 h, 54 h), as Figure 4a,c showed. And under the low-stress (500 MPa) condition, the creep life of TC25-2 (197 h) is still higher than that of TC25-1 (173 h). This indicates that the property of TC25 after heat treatment exhibits better creep resistance, as predicted. At the same temperature, the creep stress is an important parameter affecting the creep life [40]. Figure 4c indicates that the greater creep stress results in a shorter creep life and greater creep strain [11,41]. However, this phenomenon was not observed in Figure 4a, which may be caused by the microstructure and creep mechanism of titanium alloys [42].

The creep rate curves of TC25-1 and TC25-2 are presented in Figure 4b,d. It indicated that the steady-state creep rate increased with the increase in creep stress, whether before or after heat treatment. It could be found that under the same stress conditions (500 MPa, 550 MPa, 610 MPa), the steady-state creep rate of TC25-2 ($3.6 \times 10^{-8}$ $s^{-1}$, $7.2 \times 10^{-8}$ $s^{-1}$, $1.5 \times 10^{-7}$ $s^{-1}$) was lower than that of TC25-1 ($4.2 \times 10^{-8}$ $s^{-1}$, $1.1 \times 10^{-7}$ $s^{-1}$, $2.2 \times 10^{-6}$ $s^{-1}$). This phenomenon is more obvious in Figure 4e, allowing the conclusion that with the decrease in creep rate, the creep life increases. The creep mechanisms before and after heat treatment will be further discussed in Section 3.4.

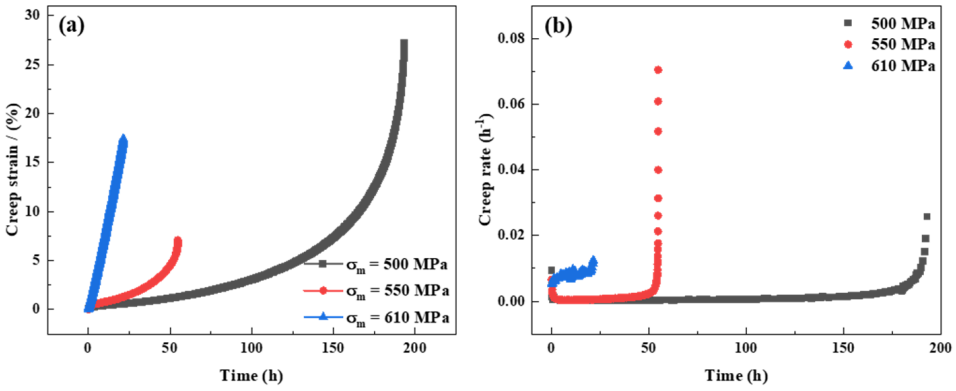


**Figure 4.** *Cont.*

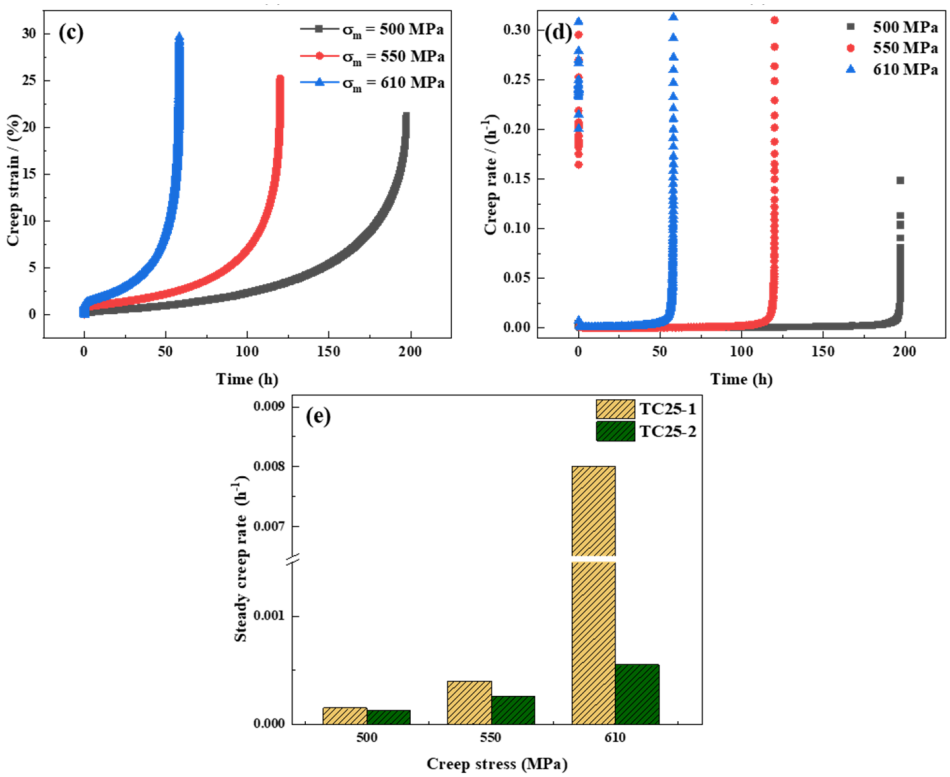


**Figure 4.** The creep properties of TC25-1 (**a**,**b**) and TC25-2 (**c**,**d**) at 550 °C: (**a**,**c**) creep curves; (**b**,**d**) creep rate curves; (**e**) steady-state creep rate.

### *3.3. Creep Fracture Mode*

Figure 5 shows the SEM morphology of TC25-1 after the creep test under different stresses at 550 °C. The macroscopic fractures (Figure 5(a1–a3)) indicate that no obvious necking behavior occurred under different stresses. Meanwhile, the shear lip regions similar to tensile fractures can be observed [28]. The microstructure in typical microregions of each group (Figure 5(b1–d1,b2–d2,b3–d3)) indicate that under three different stress conditions, the alloy exhibits a typical ductile fracture, with a large number of dimples of different sizes distributed [39]. Equiaxed $\alpha_p$ tends to form dimples at the grain boundaries and transform into micropores [43]. Under the stress of 500 MPa, tearing ridges appeared at the edge of the dimples, indicating good toughness and plasticity of TC25-1 at this stress level. With the increase in stress, the size of tearing ridges became smaller and less obvious [42]. The appearance of the cleavage facets is usually considered as cleavage fracture, which is a characteristic of brittle fracture [42,44]. River patterns are found under different stress conditions, especially at 500 MPa (Figure 5(d1)), indicating that brittle fracture occurred during the creep fracture process. Figure 5D shows the element distribution of the blue area in Figure 5(b1), indicating that the spheroidized silicide grew further during the low-stress creep process. The Al element was often used as a stabilizing element for the α phase [26,45] while the Si element was often used as a stabilizing element for the β phase [15]. During the long-term creep process, the Si element often dynamically precipitated in the form of silicide, while the precipitation of the Al element was relatively less [46,47]. The contents of Al and Si elements in the spheroidized and grown silicide are much higher than those in the matrix, indicating that during the low-stress creep process, Al and Si elements diffused from the $\alpha_p$ to the spheroidized silicide. The creep life of TC25-1 at 500 MPa is much higher than that at 550 and 610 MPa (Figure 4a), indicating the silicon element mainly dynamically precipitated in the form of silicide and interacted with dislocations to improve the creep strength [46]. These results reveal that the creep fracture of TC25-1 is a mode combining brittle fracture and ductile fracture. Under low stress, element segregation is more likely to occur, and the characteristics of brittle fracture are more obvious.

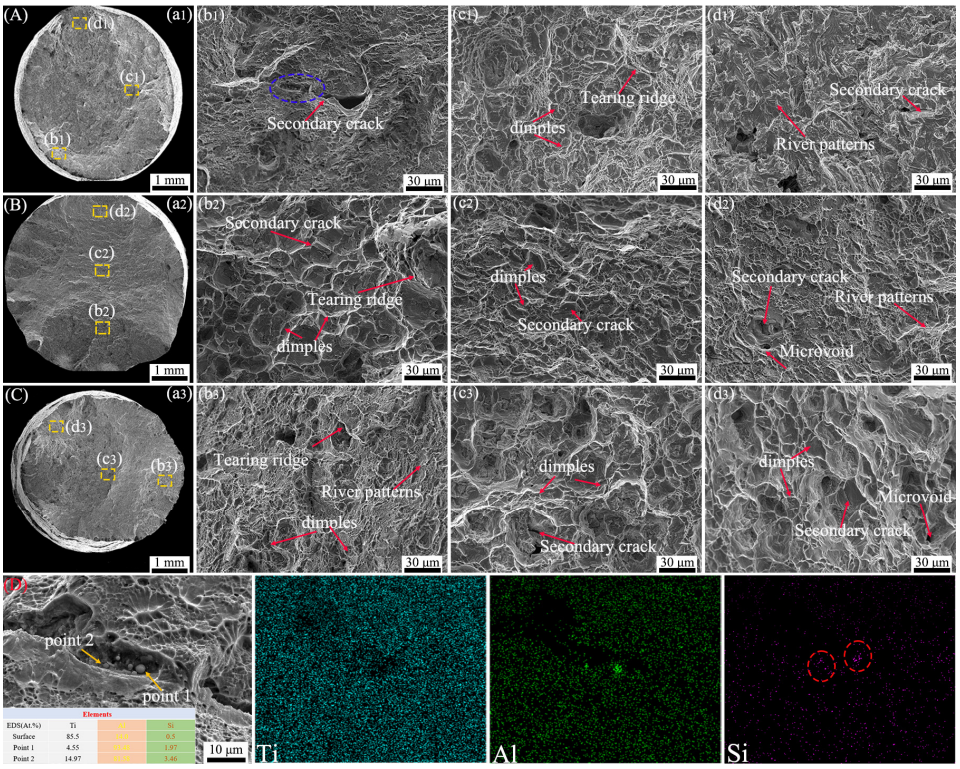


**Figure 5.** SEM creep fracture morphology of TC25-1 after creep tests (**A**) 500 MPa, (**B**) 550 MPa, (**C**) 610 MPa: (**a1**–**a3**) macroscopic fracture morphology; (**b1**–**d1**), (**b2**–**d2**), (**b3**–**d3**) morphological characteristics of typical microregions; (**D**) elemental mapping in the blue area of (**b1**).

Figure 6 shows the creep fracture surfaces of TC25-2 under different stresses at 550 °C. Figure 6(a1–c1) indicate that necking behavior occurs under different stress conditions, and the necking phenomenon becomes more pronounced with increasing stress compared with the TC25-1. This is consistent with the elongation of the specimen in the creep curves (Figure 4c). Overall, the creep fracture mode of TC25-2 is the same as that of TC25-1, which is a ductile fracture with micropore aggregation, accompanied by a large number of ductile dimples with different sizes. By comparing the tearing ridges near the dimples of the creep fracture surfaces of TC25-1 and TC25-2, it can be found that the tearing ridges of TC25-2 are more obvious, indicating that TC25-2 had a larger strain during the creep resistance process. In addition, around the dimples of TC25-2, there are a large number of microvoids, which are more than that of TC25-1, indicating that during the creep process, TC25-2 can disperse the stress, delay the crack initiation, and then have better creep resistance. In typical microscopic regions (Figure 6(b1,b2,c2), secondary cracks can be found. The secondary cracks after heat treatment are relatively fewer and shorter, indicating that it is difficult for cracks to initiate and propagate in the TC25-2 specimens. TC25-2 has smaller $\alpha_s$, which can prevent the transfer of cracks between different phases, thus having better creep resistance [48]. This was similar to basket-weave structures having better creep resistance [11]. In the microscopic regions of the creep fracture surfaces under different stresses (Figure 6(d1–d3)), the same river patterns as TC25-1 can be observed, indicating that brittle fracture is the fracture mode. However, the stress condition with obvious brittle fracture characteristics is 550 MPa, instead of 500 MPa for TC25-1. After heat treatment, the $\alpha/\beta$ interface of TC25-2 became smooth, the element distribution was more uniform, and no spheroidized β phase is found during the creep process. The above results show that the TC25-2 fracture mode is a mixed mode of ductile fracture and brittle fracture, with ductile fracture as predominating, and the refined $\alpha_s$ phase exhibits better creep resistance.

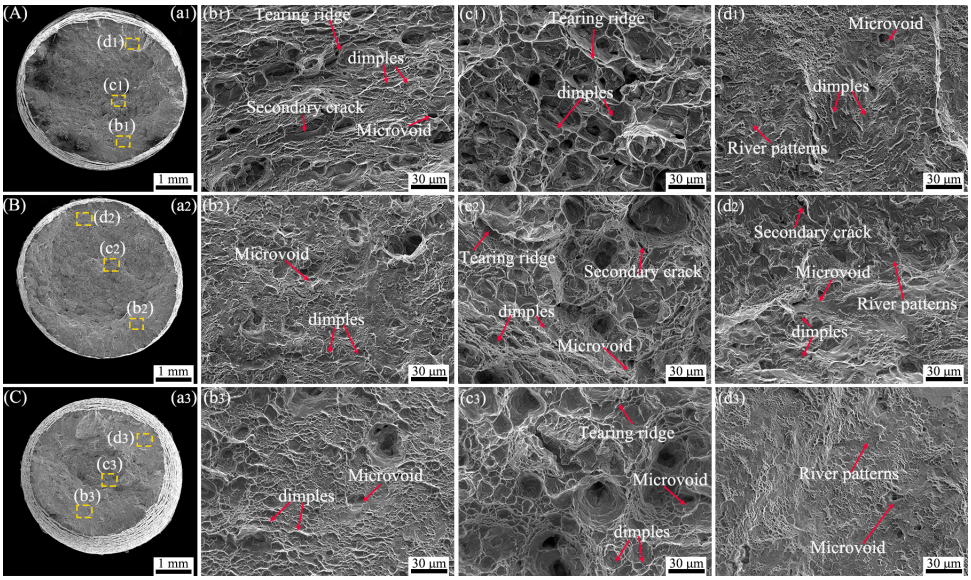


**Figure 6.** SEM creep fracture morphology of TC25-2 after creep tests at (**A**) 500 MPa, (**B**) 550 MPa, (**C**) 610 MPa: (**a1**–**a3**) macroscopic fracture morphology; (**b1**–**d1**), (**b2**–**d2**), (**b3**–**d3**) morphological characteristics of typical microregions.

### *3.4. Creep Mechanism*

According to the creep curves and creep performance results of TC25-1 and TC25-2, the steady-state creep rate is affected by the applied stress. The Arrhenius power law creep equation was used to evaluate the relationship between the steady-state creep rate and stress [15,49,50].

$$\dot{\varepsilon}_s = A\sigma^n \exp\left(-\frac{Q_s}{RT}\right) \quad (1)$$

where $\dot{\varepsilon}_s$ is steady-state creep rate ($s^{-1}$), A is the material constant, σ is flow stress (MPa), $n$ is the apparent stress index, $Q_s$ is creep apparent activation energy (KJ/mol), R is the gas constant (8.314 J/(mol K)), and $T$ is Kelvin temperature (K). The deformation mechanism of the creep process can be expressed by the apparent stress index n. Equation (1) is applicable to the case where the apparent activation energy is equal to the activation energy of metal self-diffusion [15]. According to Equation (1), the expression of n can be derived as Equation (2), as follows:

$$n = \left(\frac{\partial ln\dot{\varepsilon}}{\partial ln\sigma}\right)_T \quad (2)$$

Figure 7 shows the curves of the natural logarithmic creep steady-state rate versus stress of TC25-1 and TC25-2 at 550 °C. Usually, $n$ = 1 indicates that the creep process is controlled by the diffusion of vacancies along the grain boundaries [51]; $n$ = 2–3 indicates that the creep process is controlled by the diffusion of vacancies and dislocation climb [31,50]; $n$ = 4–8 indicates that the creep process is controlled by dislocation climb [52]. As shown in Figure 7, the apparent stress index $n$ of TC25-1 and TC25-2 is calculated to be 20.13 and 7.25, respectively, by using OriginPro 2024 software. It indicates that the creep mechanism of TC25-2 is dislocation climb. Dislocations may slide within the $\alpha_p$ and accumulate at the $\alpha_p/\beta_{trans}$ grain boundaries. However, the apparent stress index $n$ of TC25-1 is much greater than 8, indicating that there are factors hindering creep in the material before heat treatment near 550 °C [42]. By comparing the apparent stress index of TC25-1 and TC25-2, it could be found that the n value before heat treatment is much greater than that after heat treatment, indicating that TC25-1 is more sensitive to creep stress. The creep mechanisms before and after heat treatment are further analyzed below through the microstructure near the creep fracture and EBSD.

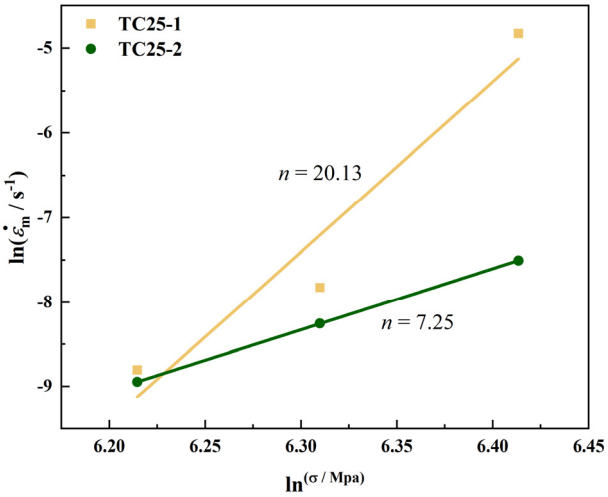


**Figure 7.** The relationship of steady-state creep rate and logarithm of stress.

The scanning electron microscope secondary electron (SE) images of the microstructures near creep fracture regions of TC25-1 and TC25-2 are shown in Figure 8. The $\alpha_p$ of TC25-1 after creep test presents obvious tensile traces in the stress loading direction. Its main deformation region is circled with a red square in Figure 8a. The tensile traces in Figure 8b are more obvious, indicating that lattice torsion occurred in the $\alpha$ phase during the creep process. In addition, obvious cracking occurs at the grain boundary of $\alpha_p/\beta_{trans}$, indicating that during the creep process, the fracture first starts from the grain boundary, and the creep mechanism is grain boundary sliding. It has been found in many studies that grain boundary sliding is a common creep mechanism in titanium alloys [17,21]. The larger microcracks formed at the convex interface of $\alpha_{p/}\beta_{trans}$ could be found, and they gradually expand to both sides, eventually causing grain boundary cracking, forming large cracks, and finally leading to creep fracture. This is consistent with the large cracks observed in the creep fracture surface (Figure 5).

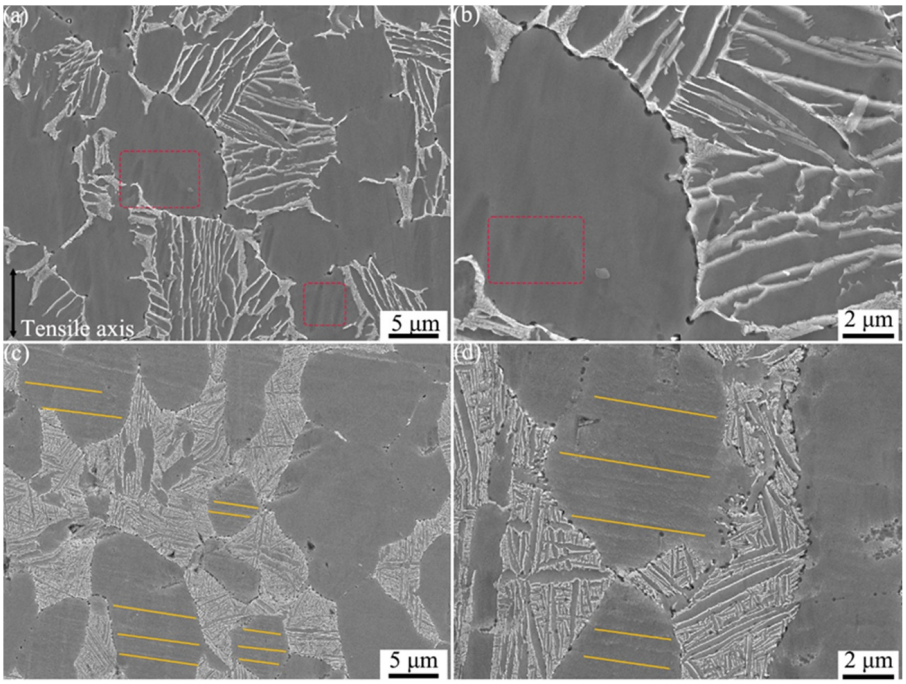


**Figure 8.** SEM images of the regions near the creep fracture at 550 °C/550 MPa: (**a**,**b**) TC25-1, (**c**,**d**) TC25-2.

Compared with TC25-1, no obvious tensile traces are observed in TC25-2, indicating that the creep mechanism changed after heat treatment. On the contrary, many slip lines perpendicular to the grain boundary of $\alpha_p/\beta_{trans}$ are found in Figure 8c, indicating that a large number of dislocations occurred during the creep process of TC25-2. The dislocations slipped along the $\alpha_p$ matrix, forming parallel slip lines [53,54]. The slip lines of the substrate are more obvious in Figure 8d, indicating that the creep mechanism of TC25-2 is dislocation climb, which is consistent with the derivation result of the Arrhenius power law creep equation. It is worth noting that no obvious slip lines are observed in the large $\alpha_p$ phase, which is caused by the Burger vector being parallel to the sample surface and the underdeveloped slip bands. It can be observed from Figure 8c that the slip lines originated from the interior of the $\alpha_p$ phase rather than the $\alpha_p/\beta_{trans}$ interface, and the slip lines terminated at the $\alpha_p/\beta_{trans}$ interface without crossing the grain boundary. Compared with the microstructure of TC25-2 before creep (Figure 3f), obvious fragmentation occurred at the $\alpha_p/\beta_{trans}$ grain boundary. Cracks formed between the interfaces of the fragmented $\alpha_p$ and β ligaments and did not exhibit aggregative behavior. This indicates that during the creep process, in order to adapt to the large creep stress and avoid stress concentration, the β ligaments are fragmented, thus resulting in better creep performance. The fragmented β ligaments would further form large dimples during the creep process (Figure 6), which is not found in TC25-1. This indicates that the structure of the grain boundary has a significant influence on the creep performance [55]. In this study, the smooth grain boundary structure has better creep performance. The refined $\alpha_s$ interface of TC25-1 also presents tiny pores (Figure 8d), indicating that the $\alpha_s$ prevents the concentration of stress and enhances the creep resistance during the creep process, which is not found in TC25-1.

Kernel average misorientation (KAM) maps can be used to characterize the stress distribution and geometric dislocation density distribution of the specimen during the deformation process [20,56]. Therefore, in order to further analyze the creep mechanisms of TC25 before and after heat treatment, KAM maps were used to characterize the dislocation distribution to a certain extent. Figure 9 shows the dislocation distribution in the vicinity after the creep fracture of TC25-1 and TC25-2. The area with a higher KAM value indicates higher stress and a greater geometric necessary dislocation density. In Figure 9a, the stress concentration area is mainly at the grain boundaries of $\alpha_p/\beta_{trans}$, indicating that dislocations mainly accumulate at the grain boundaries of $\alpha_p/\beta_{trans}$. This is prone to cause grain boundary sliding and further leads to grain boundary cracking, which is consistent with the phenomenon observed in Figure 8a. In addition, the red elliptical area in Figure 9a indicates that dislocations present a continuous banded distribution at grain boundaries of $\alpha_p/\beta_{trans}$, thereby causing cracks to propagate along the interface in TC25-1 (Figure 8b). On the contrary, in Figure 9b, the stress concentration area appeared not only at the grain boundaries of $\alpha_p/\beta_{trans}$ but also in $\alpha_s$ (red circle), indicating that the stress distribution during the creep process of TC25-2 is relatively uniform and could well improve the creep resistance. Furthermore, the fragmentation occurs in the β ligaments with a point-like dislocation distribution in the fragmented area (purple elliptical circle), which indicates that the β ligaments fragmented to further improve the creep resistance in order to adapt to the high-stress condition during the creep process. The stress concentration behavior can also be obviously observed in the small $\alpha_p$ (red square frame), which is consistent with the phenomenon in Figure 8c. The above results indicate that the creep mechanism of TC25 is grain boundary sliding before heat treatment and dislocation climb after heat treatment, and the improvement of creep performance after heat treatment mainly originated from the smooth $\alpha_p/\beta_{trans}$ grain boundary and the refined $\alpha_s$.

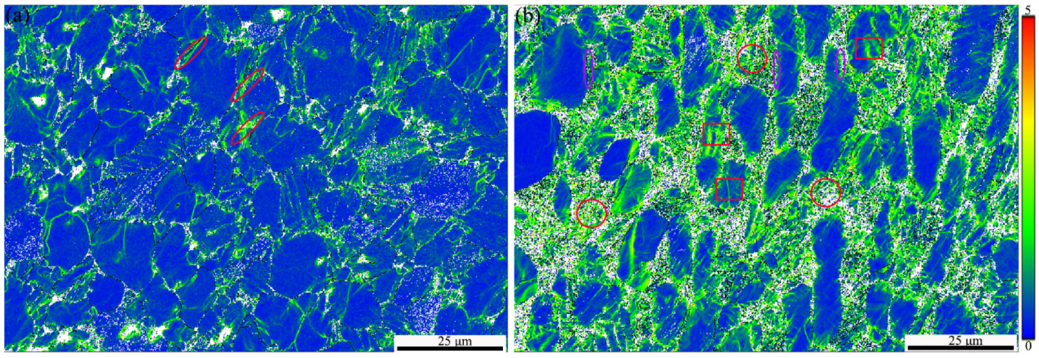


**Figure 9.** Kernel average misorientation (KAM) analysis near the creep fracture at 550 °C/550 MPa: (**a**) TC25-1, (**b**) TC25-2.

## 4. Conclusions

In summary, the microstructure changes, creep properties, and creep mechanism of the TC25 high-temperature alloy before and after heat treatment were studied. The TC25 high-temperature alloy exhibited a typical bimodal microstructure. After solution treatment (960 °C/2 h/AC) and aging treatment (550 °C/3 h/AC), the $\alpha_p/\beta_{trans}$ grain boundaries of TC25 became smoother, and the αs became finer. Heat treatment greatly improved the creep resistance of TC25, especially under high- and medium-stress conditions. Its creep life increased by approximately twice compared to that before heat treatment. At the same temperature (550 °C), the increase in stress would accelerate the creep process, resulting in a decrease in creep life and an increase in the steady-state creep rate. The main reason for the enhancement of creep resistance after heat treatment was attributed to the fact that the smooth $\alpha_p/\beta_{trans}$ grain boundaries broke during the creep process, dispersed the creep stress, and prevented dislocation climb, and the refined $\alpha_s$ could effectively prevent the dislocation movement. The creep fracture modes of TC25 before and after heat treatment are both mixed fractures combining ductile fracture and brittle fracture. The creep mechanism before heat treatment is grain boundary sliding, and the creep mechanism changed to dislocation climb after heat treatment.

**Author Contributions:** A.T., writing—review and editing, project administration, methodology, funding acquisition, conceptualization. J.M., resources, writing—original draft, methodology, investigation, formal analysis, data curation, conceptualization. Z.L., writing—review and editing, methodology, funding acquisition, conceptualization. G.K., writing—review and editing, methodology, funding acquisition, conceptualization. J.G., data curation, conceptualization. X.H., data curation, conceptualization. G.L., writing—review and editing, data curation. All authors have read and agreed to the published version of the manuscript.

**Funding:** This work was supported by the Basic Scientific Research Foundation of Central College (N2425015).

**Institutional Review Board Statement:** Not applicable.

**Informed Consent Statement:** Not applicable.

**Data Availability Statement:** The raw/processed data required to reproduce these findings cannot be shared at this time as the data also forms part of an ongoing study.

**Acknowledgments:** Authors acknowledge the support from the Basic Scientific Research Foundation of Central College (N2425015).

**Conflicts of Interest:** The authors declare no conflicts of interest.

## References


1. Xu, L.; Zheng, Y.; Liang, Z.; Tian, Y.; Yang, J.; Wang, X.; Xiao, X.; Xue, X.; Tian, J. Impact of long-term thermal exposure on the microstructure and creep resistance of (TiB+TiC+$Y_2O_3$)/α-Ti composite. *J. Alloys Compd.* **2024**, *990*, 174496. [CrossRef]
2. Yamabe-Mitarai, Y.; Yanao, K.; Toda, Y.; Ohnuma, I.; Matsunaga, T. Phase stability of Ti-containing high-entropy alloys with a bcc or hcp structure. *J. Alloy. Compd.* **2022**, *911*, 164849. [CrossRef]
3. Zhong, X.; Deng, T.; Xiao, W.; Liu, X.; Liu, Z.; Yang, Y.; Ojo, O.A. Improving thermal stability and creep resistance by Sc addition in near-α high-temperature titanium alloy. *J. Mater. Sci. Technol.* **2023**, *183*, 1–11. [CrossRef]
4. Li, J.; Cai, J.; Xu, Y.; Xiao, W.; Huang, X.; Ma, C. Influences of thermal exposure on the microstructural evolution and subsequent mechanical properties of a near-α high temperature titanium alloy. *Mater. Sci. Eng. A* **2020**, *774*, 138934. [CrossRef]
5. Wang, H.; Tan, C.; Zhao, J.; Han, L.; Zhang, G. Effect of creep stress on the high-temperature tensile stability of TC11 titanium alloy. *J. Mater. Sci.* **2023**, *58*, 5503–5515. [CrossRef]
6. Zheng, Y.; Xu, L.; Yu, J.; Liang, Z.; Xue, X.; Xiao, S.; Tian, J.; Chen, Y. Effect of TiB, TiC and $Y_2O_3$ on tensile properties and creep behavior at 650 °C of titanium matrix composites. *J. Alloys Compd.* **2022**, *908*, 164699. [CrossRef]
7. Davies, P.; Pederson, R.; Coleman, M.; Birosca, S. The hierarchy of microstructure parameters affecting the tensile ductility in centrifugally cast and forged Ti-834 alloy during high temperature exposure in air. *Acta Mater.* **2016**, *117*, 51–67. [CrossRef]
8. Wang, T.; Li, B.; Wang, Z.; Nie, Z. A microstructure with improved thermal stability and creep resistance in a novel near-alpha titanium alloy. *Mater. Sci. Eng. A* **2018**, *731*, 12–20. [CrossRef]
9. Banerjee, D.; Williams, J.C. Perspectives on Titanium Science and Technology. *Acta Mater.* **2013**, *61*, 844–879. [CrossRef]
10. Yue, K.; Liu, J.; Zhang, H.; Yu, H.; Song, Y.; Hu, Q.; Wang, Q.; Yang, R. Precipitates and alloying elements distribution in near α titanium alloy Ti65. *J. Mater. Sci. Technol.* **2019**, *36*, 91–96. [CrossRef]
11. Nie, X.; Liu, H.; Zhou, X.; Yi, D.; Huang, B.; Hu, Z.; Xu, Y.; Yang, Q.; Wang, D.; Gao, Q. Creep of Ti–5Al–5Mo–5V–1Fe–1Cr alloy with equiaxed and lamellar microstructures. *Mater. Sci. Eng. A* **2016**, *651*, 37–44. [CrossRef]
12. Lütjering, G. Influence of processing on microstructure and mechanical properties of (α+β) titanium alloys. *Mater. Sci. Eng. A* **1998**, *243*, 32–45. [CrossRef]
13. Ponsonnet, L.; Quesne, C.; Penelle, R. Microstructure and creep deformation of a near beta titanium alloy 'β-CEZ'. *Mater. Sci. Eng. A* **1999**, *262*, 50–63. [CrossRef]
14. Evans, R.; Hull, R.; Wilshire, B. The effects of alpha-case formation on the creep fracture properties of the high-temperature titanium alloy IMI834. *J. Mech. Work. Technol.* **1996**, *56*, 492–501. [CrossRef]
15. Gu, Y.; Zeng, F.; Qi, Y.; Xia, C.; Xiong, X. Tensile creep behavior of heat-treated TC11 titanium alloy at 450–550 °C. *Mater. Sci. Eng. A* **2013**, *575*, 74–85. [CrossRef]
16. Chen, Z.; Xu, L.; Liang, Z.; Cao, S.; Yang, J.; Xiao, S.; Tian, J.; Chen, Y. Effect of solution treatment and aging on microstructure, tensile properties and creep behavior of a hot-rolled β high strength titanium alloy with a composition of Ti-3.5Al–5Mo–6V–3Cr–2Sn-0.5Fe-0.1B-0.1C. *Mater. Sci. Eng. A* **2021**, *823*, 141728. [CrossRef]
17. Ankem, S.; Wyatt, Z.W.; Joost, W. Advances in Low-Temperature (<0.25Tm) Creep Behavior of Single and Two-Phase Titanium Alloys. *Procedia Eng.* **2013**, *55*, 10–16. [CrossRef]
18. Mishra, H.; Ghosal, P.; Nandy, T.; Sagar, P. Influence of Fe and Ni on creep of near α-Ti alloy IMI834. *Mater. Sci. Eng. A* **2005**, *399*, 222–231. [CrossRef]
19. Ankem, S.; Margolin, H.; Greene, C.A.; Neuberger, B.W.; Oberson, P.G. Mechanical properties of alloys consisting of two ductile phases. *Prog. Mater. Sci.* **2006**, *51*, 632–709. [CrossRef]
20. Zhang, Z.; Fan, J.; Li, R.; Kou, H.; Chen, Z.; Wang, Q.; Zhang, H.; Wang, J.; Gao, Q.; Li, J. Orientation dependent behavior of tensile-creep deformation of hot rolled Ti65 titanium alloy sheet. *J. Mater. Sci. Technol.* **2020**, *75*, 265–275. [CrossRef]
21. Fan, R.-L.; Wu, Y.; Chen, M.-H.; Xie, L.-S. Relationship among microstructure, mechanical properties and texture of TA32 titanium alloy sheets during hot tensile deformation. *Trans. Nonferrous Met. Soc. China* **2020**, *30*, 928–943. [CrossRef]
22. Oberson, P.G.; Ankem, S. The effect of time-dependent twinning on low temperature (<0.25∗Tm) creep of an alpha-titanium alloy. *Int. J. Plast.* **2009**, *25*, 881–900.
23. Xu, X.; Ding, H.; Huang, H.; Liang, H.; Guo, H.; Chen, R.; Guo, J.; Fu, H. Twin and twin intersection phenomena in a creep deformed microalloyed directionally solidified high Nb containing TiAl alloy. *J. Mater. Sci. Technol.* **2022**, *127*, 115–123. [CrossRef]
24. He, S.; Zeng, W.; Xu, J.; Chen, W. The effects of microstructure evolution on the fracture toughness of BT-25 titanium alloy during isothermal forging and subsequent heat treatment. *Mater. Sci. Eng. A* **2018**, *745*, 203–211. [CrossRef]
25. Ma, X.; Zeng, W.; Tian, F.; Zhou, Y.; Sun, Y. Optimization of hot process parameters of Ti–6.7Al–2Sn–2.2Zr–2.1Mo–1W–0.2Si alloy with lamellar starting microstructure based on the processing map. *Mater. Sci. Eng. A* **2012**, *545*, 132–138. [CrossRef]
26. Liu, X.; Zhang, X.; Du, Y.; Li, S.; Chen, H.; Li, K.; Zhao, D.; Chen, W. Insights into microstructural stability and embrittlement of TC25 high temperature titanium alloy subjected to thermal exposure. *Mater. Charact.* **2024**, *210*, 113820. [CrossRef]
27. Zhang, S.; Zeng, W.; Zhao, Q.; Gao, X.; Wang, Q. High cycle fatigue of isothermally forged Ti-6.5Al-2.2Mo-2.2Zr-1.8Sn-0.7W-0.2Si with different microstructures. *J. Alloy. Compd.* **2016**, *689*, 114–122. [CrossRef]
28. Ye, X.; Wan, M.; Huang, C.; Lei, M.; Jian, S.; Zhang, Y.; Xu, D.; Huang, F. Effect of aging temperature on mechanical properties of TC21 alloy with multi-level lamellar microstructure. *Mater. Sci. Eng. A* **2022**, *840*, 142825. [CrossRef]

29. Gu, K.; Zhao, B.; Weng, Z.; Wang, K.; Cai, H.; Wang, J. Microstructure evolution in metastable β titanium alloy subjected to deep cryogenic treatment. *Mater. Sci. Eng. A* **2018**, *723*, 157–164. [CrossRef]
30. Jian, Y.A.N.G.; Limei, P.A.N.; Xiangxin, X.U.E.; Mei, W.A.N.G.; Tai, Q.I.U. Effect of $Tb_2O_3$ additive on structure of anatase and photocatalytic activity of $TiO_2/(O' + \beta')$-Sialon multi-phase ceramics. *J. Rare Earths* **2009**, *27*, 204–210.
31. Wang, Y.; Sun, Z.; Yin, Z.; Yin, L.; Huang, L. Formation and characteristics of bilamellar microstructure in Ti6242S titanium alloy under dual heat treatment. *Mater. Charact.* **2022**, *187*, 111835. [CrossRef]
32. Liu, X.; Cui, W.; Wang, Y.; Long, Y.; Liu, F.; Liu, Y. Effects of Heat Treatment on the Microstructure Evolution and Mechanical Properties of Selective Laser Melted TC4 Titanium Alloy. *Metals* **2022**, *12*, 702. [CrossRef]
33. Lunt, D.; Xu, X.; Busolo, T.; da Fonseca, J.Q.; Preuss, M. Quantification of strain localisation in a bimodal two-phase titanium alloy. *Scr. Mater.* **2018**, *145*, 45–49. [CrossRef]
34. Han, J.; Xiang, Z.; Ma, X.; Zhou, Z.; Huang, J.; Li, J.; Wang, A.; Shen, G.; Chen, Z. Evolution on the Microstructure and Mechanical Properties of a New Multicomponent Near-Alpha Titanium Alloy after Rolling and Heat Treatments. *Metals* **2023**, *13*, 1231. [CrossRef]
35. Zhao, D.; Fan, J.-K.; Zhang, Z.-X.; Wang, J.; Wang, Q.J.; Chen, Z.Y.; Tang, B.; Kou, H.; Li, J. Influence of α+β solution treatments on Ti65 ultrathin sheets: Silicide precipitation, mechanical behaviour and novel{101¯1}twinning system. *Trans. Nonferrous Met. Soc. China* **2023**, *33*, 1098–1113. [CrossRef]
36. Su, Y.; Hao, G.; Fan, H.; Zhai, Y.; Kong, F.; Wang, X.; Chen, Y. Study on rolling of a new near-α titanium alloy: Microstructure refinement and dual-scale silicides evolution. *J. Alloy. Compd.* **2020**, *852*, 156867. [CrossRef]
37. Zhang, G.; Liu, W.; Zhang, P.; Xiong, H.; Gao, J.; Yu, H.; Yuan, H. Chemical Composition, Microstructure, Tensile and Creep Behavior of Ti60 Alloy Fabricated via Electron Beam Directed Energy Deposition. *Materials* **2022**, *15*, 3109. [CrossRef]
38. Jiao, Y.; Huang, L.; Wei, S.; Peng, H.; An, Q.; Jiang, S.; Geng, L. Constructing two-scale network microstructure with nano-Ti5Si3 for superhigh creep resistance. *J. Mater. Sci. Technol.* **2019**, *35*, 1532–1542. [CrossRef]
39. Singh, G.; Satyanarayana, D.V.V.; Pederson, R.; Datta, R.; Ramamurty, U. Enhancement in creep resistance of Ti–6Al–4V alloy due to boron addition. *Mater. Sci. Eng. A* **2014**, *597*, 194–203. [CrossRef]
40. Zeng, L.Y.; Zhao, Y.Q.; Mao, X.N.; Hong, Q.; Qi, Y.L. Creep Features of Ti-600 Alloy at the Temperature of 650 °C. *Mater. Sci. Forum.* **2018**, *941*, 995–1003. [CrossRef]
41. Zhang, M.; Qiu, J.; Fang, C.; Zhang, M.; Ma, Y.; Yang, Z.; Lei, J.; Yang, R. Room temperature creep mechanisms of Ti–6Al–4V ELI alloy with equiaxed microstructure under different applied stresses. *J. Mater. Res. Technol.* **2023**, *27*, 1579–1592. [CrossRef]
42. Yao, M.; Yao, Z.; Yi, C.; Moliar, O.; Soloviova, T.; Trosnikova, I.; Yurkova, A.; Loboda, P.; Zhang, S. Microstructure and creep behavior of electron beam directed energy deposited TC11 titanium alloy. *Mater. Sci. Eng. A* **2024**, *913*, 147020. [CrossRef]
43. Wang, J.; Zhao, Y.; Zhao, Q.; Lei, C.; Zhou, W.; Zeng, W. In-Situ Study on Tensile Deformation and Fracture Mechanisms of Metastable β Titanium Alloy with Equiaxed Microstructure. *Materials* **2022**, *15*, 1325. [CrossRef]
44. Zheng, Z.; Kong, F.; Chen, Y.; Wang, X. Effect of nano-$Y_2O_3$ addition on the creep behavior of an as-cast near-α titanium alloy. *Mater. Charact.* **2021**, *178*, 111249. [CrossRef]
45. Dichtl, C.; Zhang, Z.; Gardner, H.; Bagot, P.; Radecka, A.; Dye, D.; Thomas, M.; Sandala, R.; Fonseca, J.Q.; Preuss, M. Element segregation and α2 formation in primary α of a near-α Ti-alloy. *Mater. Charact.* **2020**, *164*, 110327. [CrossRef]
46. Viswanathan, G.; Karthikeyan, S.; Hayes, R.; Mills, M. Creep behaviour of Ti-6Al-2Sn-4Zr-2Mo: II. Mechanisms of deformation. *Acta Mater.* **2002**, *50*, 4965–4980. [CrossRef]
47. Tsuyama, S.; Mitao, S.; Minakawa, K.N. Alloy modification of γ-base titanium aluminide for improved oxidation re-sistance, creep strength and fracture toughness. *Mater. Sci. Eng. A* **1992**, *153*, 451–456. [CrossRef]
48. Li, S.; Deng, T.; Zhang, Y.; Liang, Y.; Li, R.; Dong, T. Review on the Creep Resistance of High-Temperature Titanium Alloy. *Trans. Indian Inst. Met.* **2021**, *74*, 215–222. [CrossRef]
49. Panicker, R.; Chokshi, A.; Mishra, R.; Verma, R.; Krajewski, P. Microstructural evolution and grain boundary sliding in a superplastic magnesium AZ31 alloy. *Acta Mater.* **2009**, *57*, 3683–3693. [CrossRef]
50. Zhang, Y.; Li, D.; Li, X.; Liu, X.; Zhao, S.; Li, Y. Creep deformation and strength evolution mechanisms of a Ti-6Al-4V alloy during stress relaxation at elevated temperatures from elastic to plastic loading. *J. Mater. Sci. Technol.* **2022**, *126*, 93–105. [CrossRef]
51. Tong, Y.; Qiao, J.; Yao, Y. The constitutive model and threshold stress for characterizing the deformation mechanism of Al0.3CoCrFeNi high entropy alloy. *Mater. Sci. Eng. A* **2018**, *730*, 137–146. [CrossRef]
52. Li, H.; Bian, T.-J.; Lei, C.; Zheng, G.-W.; Wang, Y.-F. Dynamic interplay between dislocations and precipitates in creep aging of an Al-Zn-Mg-Cu alloy. *Adv. Manuf.* **2018**, *7*, 15–29. [CrossRef]
53. Zhang, W.; Fan, J.; Huang, H.; Xue, X.; Wang, Y.; Zhang, B.; Jiang, P.; Wang, C.; Kou, H.; Li, J. Creep anisotropy characteristics and microstructural crystallography of marine engi-neering titanium alloy Ti6321 plate at room temperature. *Mater. Sci. Eng. A* **2022**, *854*, 143728. [CrossRef]
54. Li, H.; Mason, D.E.; Yang, Y.; Bieler, T.R.; Crimp, M.A.; Boehlert, C.J. Comparison of the deformation behaviour of commercially pure titanium and Ti–5Al–2.5Sn(wt.%) at 296 and 728 K. *Philos. Mag.* **2013**, *93*, 2875–2895. [CrossRef]

55. Xin, S.W.; Zhao, Y.Q.; Lu, Y.F.; Li, Q.; Yang, H.Y. Role of grain boundaries in the high-temperature performance of a highly stabilized beta titanium alloy II: Creep behavior. *Mater. Sci. Eng. A* **2013**, *559*, 7–13. [CrossRef]
56. Liu, C.; Yu, Y.; Sun, H.; Yin, F.; Xie, L.; Qian, D.; Song, Y.; Wang, L.; Zhang, L.-C.; Hua, L. Local strain evolution near α/β interface in TC11 titanium alloy under electroshocking treatment. *Mater. Charact.* **2024**, *209*, 113689. [CrossRef]

**Disclaimer/Publisher's Note:** The statements, opinions and data contained in all publications are solely those of the individual author(s) and contributor(s) and not of MDPI and/or the editor(s). MDPI and/or the editor(s) disclaim responsibility for any injury to people or property resulting from any ideas, methods, instructions or products referred to in the content.